

# New Observations on the Brittle Failure Process of Simulated Crystalline Rocks

Hossain Noferești · K. Seshagiri Rao

Received: 11 December 2007 / Accepted: 8 June 2008 / Published online: 31 March 2009  
© Springer-Verlag 2009

**Abstract** A biaxial testing program has been performed to study the process of brittle failure in crystalline rocks. Dental plaster has been selected as a model material, and mixing with different ratios of distilled water, different types of common minerals of crystalline rocks have been simulated in the form of brick-like small elements. These elements have been interlocked together according to four systematic patterns and final specimens with  $180 \times 180 \times 76$  mm dimensions have been obtained. Details of different types of cracks observed during loading process, effects of mechanical, geometrical and confining pressure on the cracking intensity, the influence of different types of heterogeneity on the macroscopic properties of a system of interlocked elements, and the sequence of events during the failure process are presented in this paper. Based on these observations, a revised mechanism for brittle failure is proposed.

**Keywords** Brittle failure · Crystalline rocks · Interlocking · Heterogeneity · Dental plaster

## 1 Introduction

Brittle failure is a familiar phenomenon in rock mechanics, which occurs at zero or low confining pressures. Despite the remarkable development of rock mechanics in the

recent past, sufficient insight into the real mechanism of this failure type has not been achieved. In part, this has occurred because of the complexity of the subject. Even in a homogeneous, isotropic solid, treating the problem is very hard; cracks form at the atomic scale, extend to the macroscopic level, are irreversible and travel far from equilibrium. Many of the tools with which solid mechanics was built do not work (Marder and Fineberg 1996). Rocks, in turn, complicate the problem further, since they are heterogeneous and thereby anisotropic.

Experimental studies of intact rock behaviour under compressive stresses started with early fundamental researches using direct examination of the failure process under stiff testing machines such as Cook (1965) and Bieniawski (1967). Subsequent researchers focused on crack growth and interactions observed in either thin sections of rock specimens or blocks of model materials loaded in stiff or servo-controlled testing machines (among others Peng and Johnson 1972; Hallbauer et al. 1973; Nemat-Nasser and Horii 1982; Reyes and Einstein 1991). Observations of the crack initiation, propagation and coalescence in the rock specimens, loaded to different points along their stress–strain curve under high-resolution optical or scanning electron microscopes (among others Sprunt and Brace 1974; Kranz 1979; Wong 1982; Menéndez et al. 1996; Wu et al. 2000), or indirectly through the acoustic emission method (among others Lockner and Byerlee 1977; Reches and Lockner 1994; Baud et al. 2004), started in 1970s but are yet the mainstream of research these days. The following major conclusions can be derived based on the review of these research works (Noferești 2007):

1. Heterogeneities in microstructure result in local concentrations of tensile stress, even when rock is subjected only to compressive stresses. These local

---

H. Noferești (✉)  
Faculty of Engineering, University of Birjand, Birjand, Iran  
e-mail: hnoferești@birjand.ac.ir

K. S. Rao  
Department of Civil Engineering,  
Indian Institute of Technology Delhi,  
Hauz Khas, New Delhi 110016, India

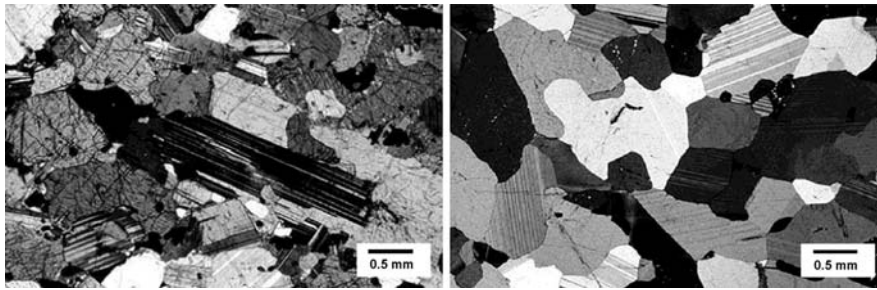


**Fig. 1** Interlocking textures of (left) an igneous rock and (right) a metamorphic rock (Reprinted from Atlas of Igneous and Metamorphic Rocks, Minerals and Textures, Virtual Geology Project,

<http://www.geosci.unc.edu/Petunia/IgMetAtlas/mainmenu.html>, University of North Carolina, with permission from Allen Glazner)

tensile stresses cause tensile cracks, sub-parallel to the maximum compression.

2. As the compressive load increases, tensile cracks become more abundant, starting at a stress close to the half of the peak strength.
3. Two important stabilising processes take place during the loading of cracks in compression. First, as cracks extend, stress intensity decreases and additional deviatoric stress must be applied to cause further crack growth. Second, diagonal flaws, which are favourably oriented to act as nucleation points for shear failure, propagate out-of-plane (parallel to  $\sigma_1$ ) and cannot maintain the necessary shear geometry.
4. At a critical moment, the crack densities become sufficiently large and therefore significant crack interactions occur, leading to the nucleation of a shear fracture that connects en-echelon arrays of the dilatant microcracks.
5. The shear fracture propagates in plane due to its own stress field. The shear tip is surrounded by a process zone, where the energy is dissipated by the growth of microcracks as fracture advances through the rock.

Despite these experimental studies as Blair and Cook (1998) pointed out, two central questions remain to be answered:

1. At which point does crack interaction overwhelm the local properties and drive the system to fracture? and,
2. What is the role of heterogeneity on the brittle failure process?

To achieve a closer view of the actual brittle failure phenomenon, an elaborate testing programme comparing to previous studies is necessary. The experimental approaches adopted so far have been focused on intact natural rocks or rock-like material. No attempts have been made in the latter case to simulate the heterogeneous and interlocked nature of rock. Using dental plaster mixed with different distilled water ratios, it was tried to create the sharp differences between the mechanical properties of the small

brick-like elements. These elements were then put together to make the large blocky specimens that were nearly heterogeneous and interlocked as observed in crystalline rocks. A detailed coverage of the experimental set-up and results of the present study are presented in the following sections.

## 2 Characteristics of the Crystalline Rocks

Crystalline rocks include mostly igneous and metamorphic rock types that expose a structure of interlocked crystals (Fig. 1). Microscopic observations (Fig. 2) have proved that no chemical bond exists among the crystals and that the overall strength of these rocks is only due to their very intricate and three-dimensional interlocking. Regarding igneous rocks, many mechanisms are suggested by geologists responsible for the mineral crystallisation from original magma. However, the most recognized mechanisms are

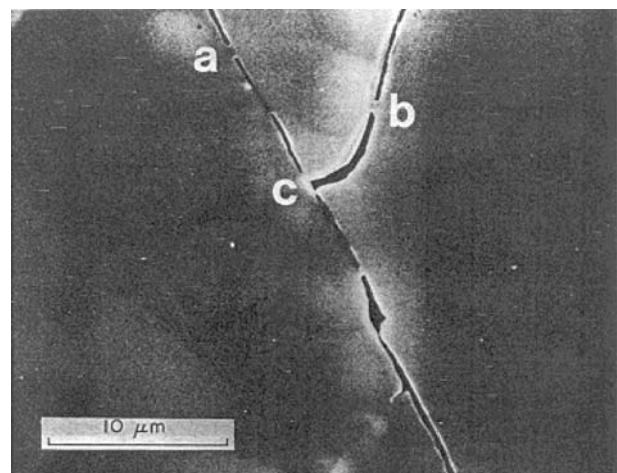
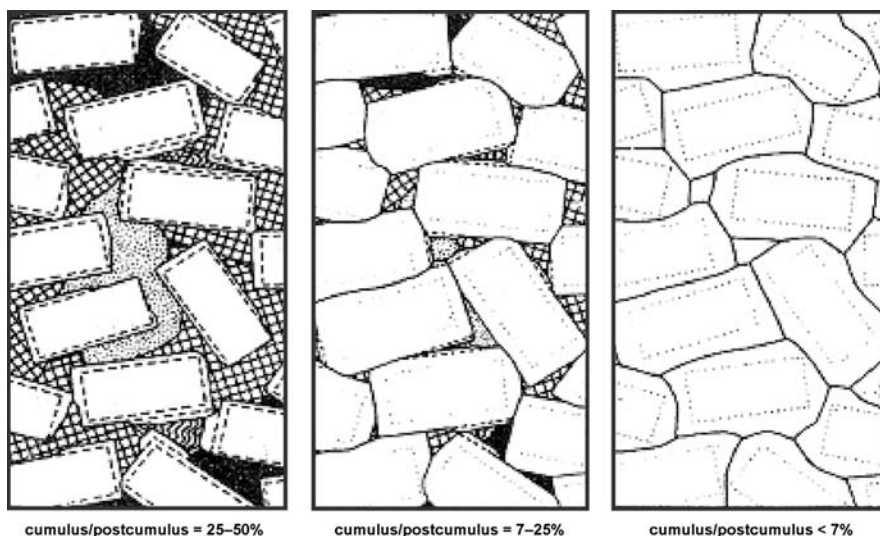


**Fig. 2** Quartz grain boundaries in Westerly Granite. Open boundaries advocate that there is no chemical bond. Small bridges at *a*, *b* and *c* suggest a late alteration or ‘healing’ of boundary cracks introduced early in the history of the rock (Reprinted from Sprunt and Brace 1974 with permission from Elsevier)

**Fig. 3** Three different types of plagioclase cumulate (Reprinted from Wager et al. 1960 with permission from Copyright Clearance Center, Rightslink)



crystal settling, first documented by Bowen (1915), and magma convection (Martin et al. 1987). But as discussed by Philpotts (1990), a combination of these mechanisms is more likely to cause igneous crystallisation.

According to Irvine (1982), igneous crystalline rocks have a characteristic texture formed by two contrasting types of mineral grains. First, there are large, roughly euhedral crystals (*cumulus grains*) that tend to rest against each other and form a framework. Between these grains are minerals that form during a *postcumulus* period (Philpotts 1990). Depending upon the percentage of these mutual parts, different types of igneous textures are formed as shown in Fig. 3. Although this figure (Wager et al. 1960) is originally proposed for plutonic rocks, it may be extended to all igneous rocks considering a larger variation in relative percentage and size of the mutual parts.

Metamorphic rocks, on the other hand, usually display a banded or foliated texture with platy or elongated crystals as a result of extreme pressure and temperature applied to them. However, metamorphic rocks such as quartzite and marble have granular texture. In addition, some of the sedimentary rocks derived from chemical precipitation (e.g. limestone, rock salt, and dolomite) may be considered as crystalline materials. These rocks are generally single-mineral with a compacted texture.

In view of the fact that most of the crystalline rocks are igneous, they were focused in further detail in this study to select a suitable model material.

### 3 Selection and Characterisation of the Model Material

Instead of directly working with crystalline rocks, use of suitable alternative that exposes strongly similar behaviour in the area of concern is tried. To select a proper model material many factors are considered, i.e. behaving in a

brittle fashion against applied stresses, easy adjustment of the mechanical properties of the model material so as to adjust for different rock forming minerals, and the ease of preparation and curing in the laboratory. Regarding the mechanical properties, uniaxial compressive strength,  $\sigma_c$ , and the elastic modulus,  $E$ , are taken into account because the first summarises the strength properties and the latter deformational behaviour of the minerals. The ratio between  $\sigma_c$  and  $E$  of the minerals is considered as the simulation parameter in the present study.

#### 3.1 Mechanical Properties of the Major Minerals in Igneous Rocks

According to Barth (1952) in almost all igneous rocks, five major minerals i.e. quartz, feldspar, mica, pyroxene and olivine are always present; the percentage of the other minerals is negligible (Table 1). The elastic modulus,  $E$ , of these minerals is calculated as follows:

$$E = 3k(1 - 2\nu) \quad (1)$$

where  $k$  is the static bulk modulus of the minerals from Knittle (1995), and  $\nu$  is the Poisson's ratios from Belikov (1967).

Regarding the compressive strength of the minerals, no reliable information was found in the literature. Thus the indirect method adopted by Dorner and Stöckhert (2004) is followed here. In this method (Johnson 1985), from the Vickers hardness number of a material one can estimate  $\sigma_c$  using the following formula:

$$H_v = 2/3 \{ 2 + \ln [ E \tan \beta_v / 6\sigma_c (1 - \nu) + 2(1 - 2\nu) / 3(1 - \nu) ] \} \sigma_c \quad (2)$$

where,  $H_v$  is the Vickers hardness number, and  $\beta_v$  is the angle between the sample surface and the indenter facet.

**Table 1** Average mineral composition of all igneous rocks (Barth, 1952)

| Mineral name            | Percentage (%) |
|-------------------------|----------------|
| Quartz                  | 12.4           |
| Alkali–feldspar         | 31.0           |
| Plagioclase             | 29.2           |
| Pyroxene                | 12.0           |
| Hornblende              | 1.7            |
| Biotite                 | 3.8            |
| Muscovite               | 1.4            |
| Olivine                 | 2.6            |
| Nepheline               | 0.3            |
| Opaque ores             | 4.1            |
| Chlorite and serpentine | 0.6            |
| Apatite                 | 0.6            |
| Sphene                  | 0.3            |
| Total                   | 100            |

**Table 2** Average mechanical properties of major minerals present in igneous rocks

| Mineral         | $\nu$ | $k$<br>GPa | $H_v$<br>GPa | $E$<br>GPa | $\sigma_c$<br>GPa | $E/E_Q$ | $\sigma_c/\sigma_{cQ}$ |
|-----------------|-------|------------|--------------|------------|-------------------|---------|------------------------|
| Quartz          | 0.09  | 37         | 10.4         | 92.1       | 6.35              | 1.00    | 1.00                   |
| Olivine         | 0.24  | 125        | 9.6          | 195        | 4.11              | 2.25    | 0.65                   |
| Plagioclase     | 0.28  | 82         | 7.8          | 108.2      | 4.30              | 0.83    | 0.66                   |
| Alkali feldspar | 0.29  | 67         | 7.2          | 84.4       | 4.14              |         |                        |
| Pyroxene        | 0.24  | 120        | 6.7          | 187.2      | 2.86              | 1.55    | 0.45                   |
| Mica (Biotite)  | 0.28  | 61.5       | 1.1          | 81.2       | 0.33              | 0.72    | 0.05                   |

Having the Vickers hardness numbers of minerals (Bruland 1998) and using Eq. 2  $\sigma_c$  values for five major minerals are calculated according to Table 2.

### 3.2 Dental Plaster as a Model Material

To find out a suitable set of compositions for simulating the major minerals of igneous rocks a variety of materials and additives were considered. After conducting around 120 uniaxial compression tests on dental plaster and in some cases plaster of Paris, white cement and red brick, it became clear that none of the tried additives can change the mechanical properties of the dental plaster so that its strength decreases while its modulus increases or vice versa. This type of adjustment is required for simulation of the same strength and modulus ratios that exist between olivine–quartz and pyroxene–quartz. Modulus of these two minerals is higher than quartz modulus while their uniaxial compressive strength is lower than quartz strength. In case of biotite, practically, the same problem exists. In comparison to quartz, its strength is very low while its modulus is as large as 70% of the quartz modulus.

**Table 3** Four model materials selected to roughly represent major mineral groups present in igneous rocks

| Model material             | $E$<br>GPa | $\sigma_c$<br>MPa | $E/E_Q$ | $\sigma_c/\sigma_{cQ}$ |
|----------------------------|------------|-------------------|---------|------------------------|
| Q (Kalstone + 35.7% water) | 6.85       | 47.1              | 1.00    | 1.00                   |
| F (Kalstone + 43% water)   | 5.5        | 36.0              | 0.80    | 0.76                   |
| P (Ultrarock + 45% water)  | 6.66       | 25.40             | 0.97    | 0.54                   |
| B (Kaldent + 70% water)    | 2.37       | 8.9               | 0.35    | 0.19                   |

Considering this fact, the simulation approach was shifted from a strict to an open approach that primarily focuses on strength ratio of the minerals and in that case tries to simulate the modulus ratio as much as possible. With this new strategy three model materials, named as Q, B, and P, were selected to represent quartz, biotite, and pyroxene respectively. Only one model material, named as F, was selected to represent both feldspar and olivine, since their strength ratios were the same and it was not possible to simulate the modulus ratio of olivine. Table 3 shows final compositions selected to simulate the rock forming minerals. As per Table 3, three varieties of dental plaster, commercially named as KALDENT, KALSTONE and ULTRAROCK produced by the Kalabhai Karson Pvt.Ltd. Mumbai India, were selected as the base powders to make four different model materials.

### 3.3 Physical and Mechanical Properties

Specific gravity (SG), dry density ( $\gamma_d$ ) and porosity ( $n$ ) as physical properties and uniaxial compressive strength ( $\sigma_c$ ), Brazilian strength ( $\sigma_t$ ), cohesion ( $c$ ), angle of internal friction ( $\varphi$ ), and Poisson's ratio ( $\nu$ ) as mechanical properties are determined for all model materials according to the procedures given by ISRM (1978, 1979) as presented in Table 4.

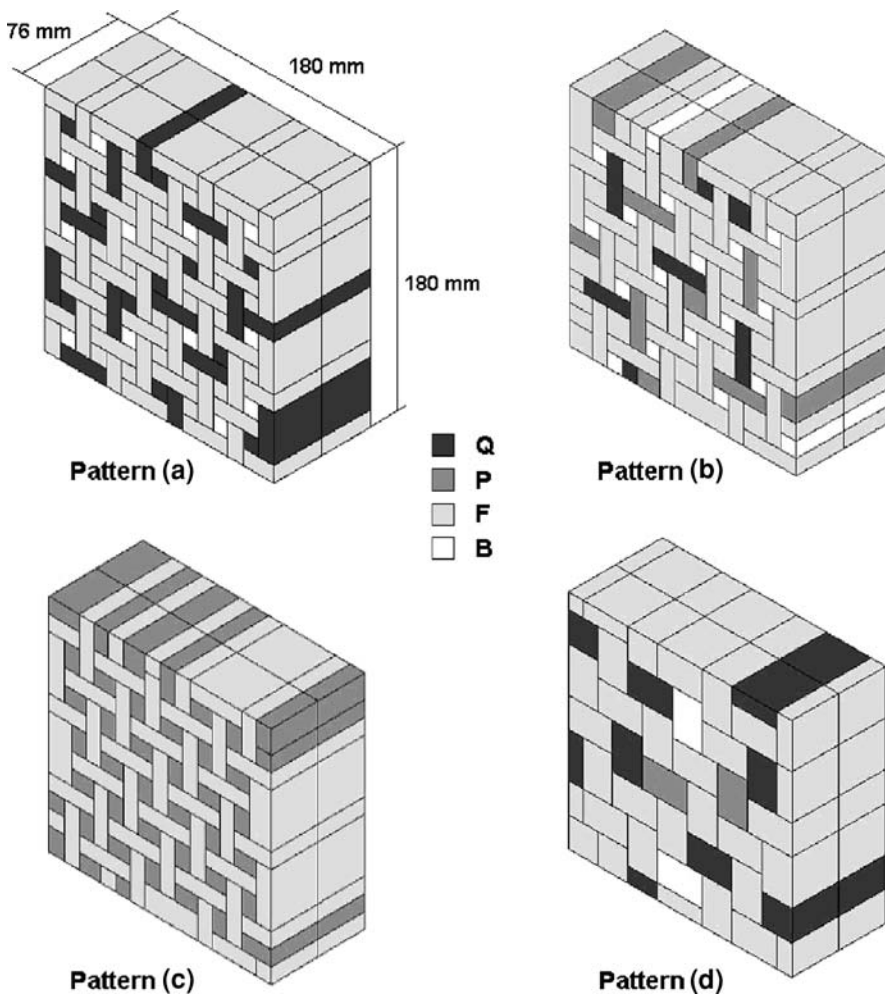
## 4 Experimental Set-up

Using four systematic interlocking patterns, i.e. patterns A, B, C and D, real interlocking textures of crystalline rocks at micro-level were simulated as shown in Fig. 4. Enlargement of the microscopic texture to a macroscopic systematic pattern is an unconventional way of modelling adopted here, making the model similar to a masonry wall. Interestingly, there are close similarities between some results of the present study and findings of the researchers working on masonry structures, which are discussed in Sect. 5.5. Using this macro-model, direct observation over sequence of events that occur during a failure process is possible. Every step in the failure process is under supervision and the vital work of making and recording experimental observations is quite easier and more reliable.

**Table 4** Summary of physical and mechanical properties of four model materials used

| Model material | $SG$ | $\gamma_d$ (g/cm <sup>3</sup> ) | $n$ (porosity) | $\sigma_c$ MPa | $E$ GPa | $c$ MPa | $\varphi^\circ$ | $\sigma_t$ MPa | $\nu$ |
|----------------|------|---------------------------------|----------------|----------------|---------|---------|-----------------|----------------|-------|
| Q              | 2.54 | 1.61                            | 0.37           | 47.1           | 6.85    | 9.9     | 44.4            | 7.42           | 0.18  |
| F              | 2.54 | 1.48                            | 0.42           | 36.0           | 5.50    | 8.3     | 40.3            | 5.44           | 0.23  |
| B              | 2.61 | 1.09                            | 0.58           | 8.9            | 2.37    | 2.2     | 37.3            | 2.07           | 0.23  |
| P              | 2.13 | 1.48                            | 0.30           | 25.4           | 6.66    | 6.1     | 38.9            | 5.55           | 0.24  |

**Fig. 4** Perspectives of four systematic patterns used to simulate the natural textures. *black Q, dark grey P, light grey F, white B*



For all systematic patterns, the overall size of the specimen was 180 × 180 × 76 mm. It was made of two layers, each having 38 mm thickness. Each layer was made of dissimilar element sizes interlocked together. In total, 18 different element sizes were used. To give a heterogeneous nature to the specimens, different element materials were used.

The building elements of the specimens were prepared by mixing the dental plaster with different distilled water ratios and then pouring the paste into split moulds (Fig. 5). The moulds consisted of two mirror parts with varying-

length strips placed in between to form the third dimension of the cast elements.

The curing was done by keeping the prepared elements at room temperature for at least 20 days. After curing, the building elements were assembled, according to the necessary pattern, into large specimens and right before testing were put in the oven for 24 h. While assembling, minor adjustments in the size and shape of the elements were made using sandpaper.

Final cured specimens were tested in biaxial loading conditions. To perform biaxial testing the 1,000 kN True

Triaxial System (TTS) developed at IIT Delhi by Rao and Tiwari (2004) was used. Very low strain rates were selected to provide sufficient time to observe and record cracking processes in the sample faces and to take proper photographs. Each test took around 30–45 min to complete.

Altogether 66 specimens were tested at four lateral pressures i.e. 0.08, 0.15, 0.88, 3.10 MPa, four interlocking patterns and with different configurations of the element types. After completion of each test, the specimen was carefully removed from the loading section and put on a table. Induced cracks on all six faces of the specimens were mapped on printed sheets.

## 5 Results and Discussion

### 5.1 Crack Shapes and Patterns

The characteristic feature of a brittle material in response to the applied load is the tensile crack initiation and further sub-parallel growth to the direction of major principal stress ( $\sigma_1$ ). In the present study, these types of cracks were observed on all faces of the specimens. According to Fig. 6, the observed tensile cracks can be roughly categorised into the following groups

1. Sharp straight tensile cracks (Fig. 6a). These cracks have the least deviation from the direction of the major principal stress.
2. Simple curved tensile cracks, are curved in one or both ends (Fig. 6b).
3. Complex curved tensile cracks, more than one curve exists along the crack (Fig. 6c).
4. Sharp-branched tensile cracks. Branching occurs along the direction of the original cracks (Fig. 6d) or against the direction of the original crack (Fig. 6e).
5. Curved-branched tensile cracks. Branching occurs along the direction of the original cracks (Fig. 6f) or against the direction of the original crack (Fig. 6g). Many branches may initiate from the original cracks (Fig. 6h).
6. Combined cracks. These cracks are actually made of two cracks that have joined with each other (Fig. 6i). Some portions of the original cracks have become inactive after joining; therefore, the complex shape of the combined cracks is more evident in the first look (Fig. 6j).

As load increases on a brittle material further tensile cracks initiate or the same cracks grow in length. But concurrently, some shear movements occur along the pre-existing and favourably oriented tensile cracks. This shear movement changes the surface condition of the tensile

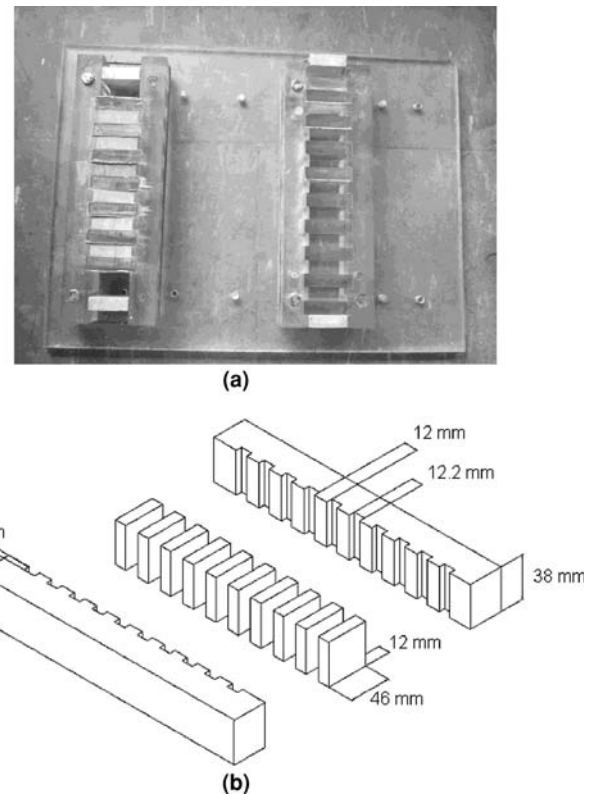


**Fig. 5** Special acrylic split moulds used to make elements of different sizes, **a** photograph and **b** schematic sketch

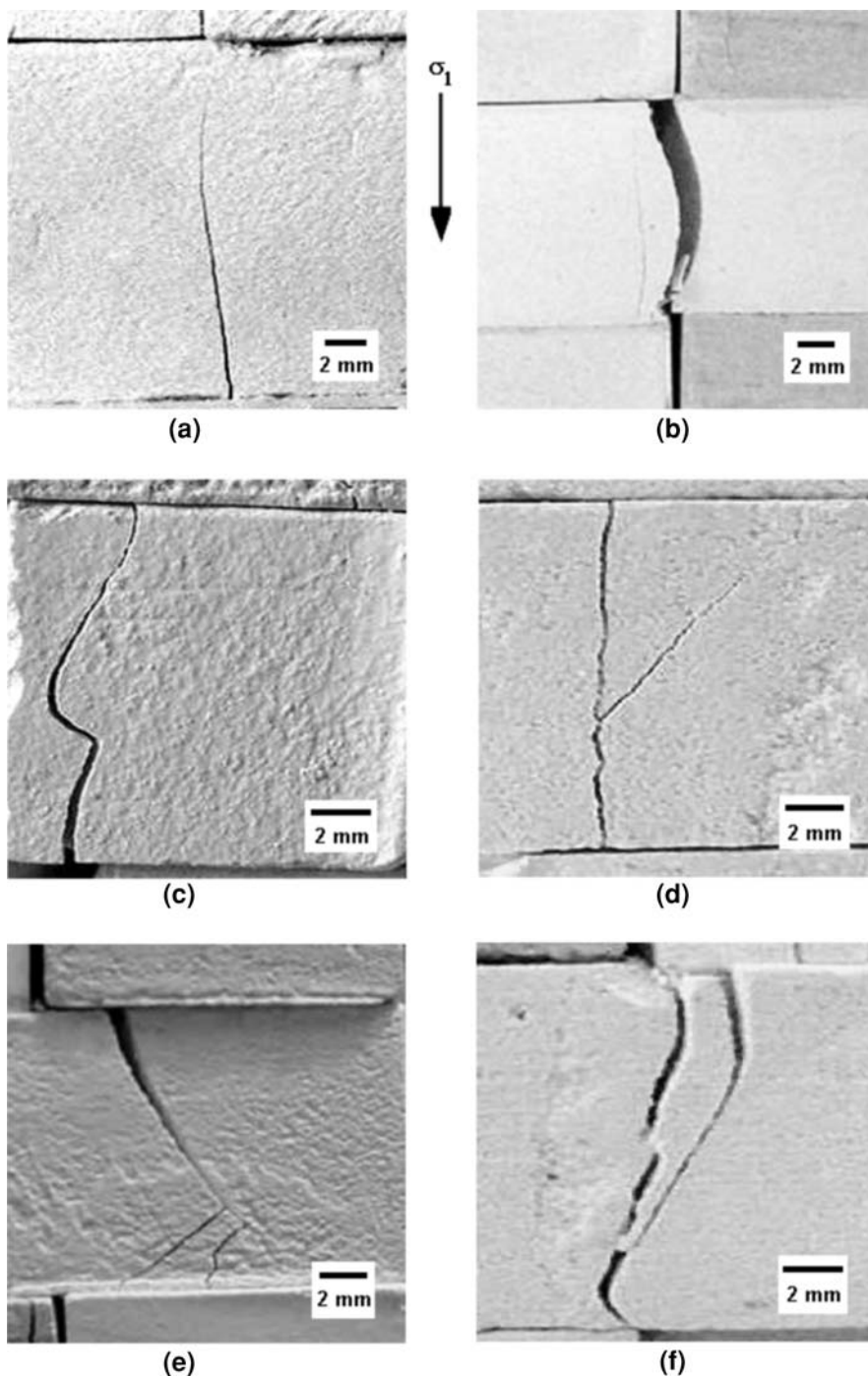
cracks from clean and sharp appearance to the earthy appearance with significant amounts of pulverised material (Fig. 7).

Essentially shear type of cracks is formed in the brittle specimens at the late stages of loading as shown in Fig. 8. One type of shear cracks, which was unique to the weaker elements of the specimens, i.e. B and P elements, is seen in Fig. 8a, b. Clear shear movement is evident in the B-element in Fig. 8a, b that implies the weak and plastic nature of the B material in comparison to the Q and F materials. Figure 8c, however, shows a completely different type of shear macrocrack that joins the very closely located tensile cracks and so forms the macroscopic failure plane. This latter type of shear cracks sometimes takes en-echelon shape as observed in this study (Fig. 18) and in conformity with the observations of Kranz (1979).

### 5.2 Analysis of Crack Densities

For each tested specimen, the crack sheet prepared after completion of the failure process was examined and the number of cracks within each element of the specimen was counted. Data were tabulated with respect to size and material type of the elements for all specimens. Based on

**Fig. 6** Different types of tensile crack observed in the present study



these data, the crack density values were calculated for each specimen and each pattern in different respects i.e. lateral pressure, material types, element size and element aspect ratio. To calculate the crack density, the following simple equation is used:

$$\rho = N/A \tag{3}$$

where,  $\rho$  is the average crack density,  $N$  is the number of cracks in similar elements, and  $A$  is the area covered by similar elements in  $m^2$ .

Having the density values, a series of analyses were performed to find out the effective parameters on crack density as an index of the damage level.

The effects of lateral pressure on the crack density was studied in all patterns. Figure 9 shows the average crack density values at different levels of lateral pressure. As shown in Fig. 9, the average crack density in a specimen decreases with increase in lateral pressure.

Effects of strength and elastic modulus of elements on the average crack density were studied for all patterns.

Fig. 6 continued

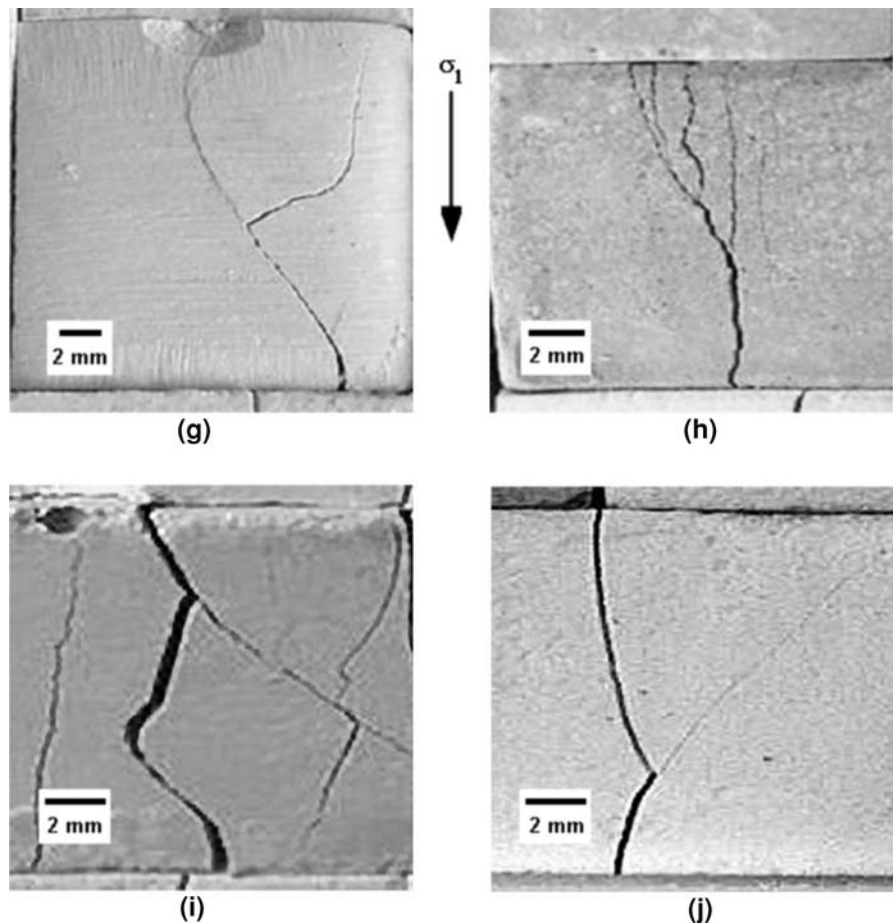


Fig. 7 Occurrence of shear movements along the surface of tensile cracks

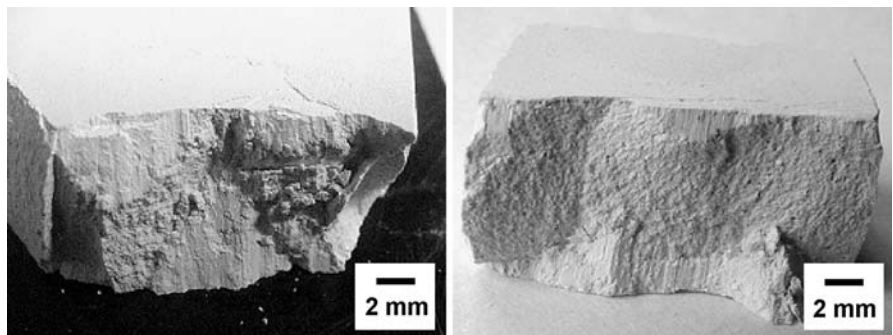


Figure 10a, b depicts these data and demonstrate a general reduction of the crack density along with increase in elemental strength and elastic modulus. An exception exists in this trend between the material types P and F. Material P has a higher elastic modulus than F, but as shown in Fig. 10b, the associated crack density for a specimen made of material P is higher than the specimen made of material F. This of course could be explained by noticing the fact that the strength of material P is lower than F. A general conclusion can be made by this observation, that the damage level in a material is primarily related to its strength value and not to the elastic modulus value.

While the above associations are more or less expectable, strong relationships are observed between crack density and geometrical factors of the building elements/grains (Figs. 11, 12). Size of the elements is observed to affect the damage level, i.e. crack density at failure decreases for larger elements following a negative power law equation:

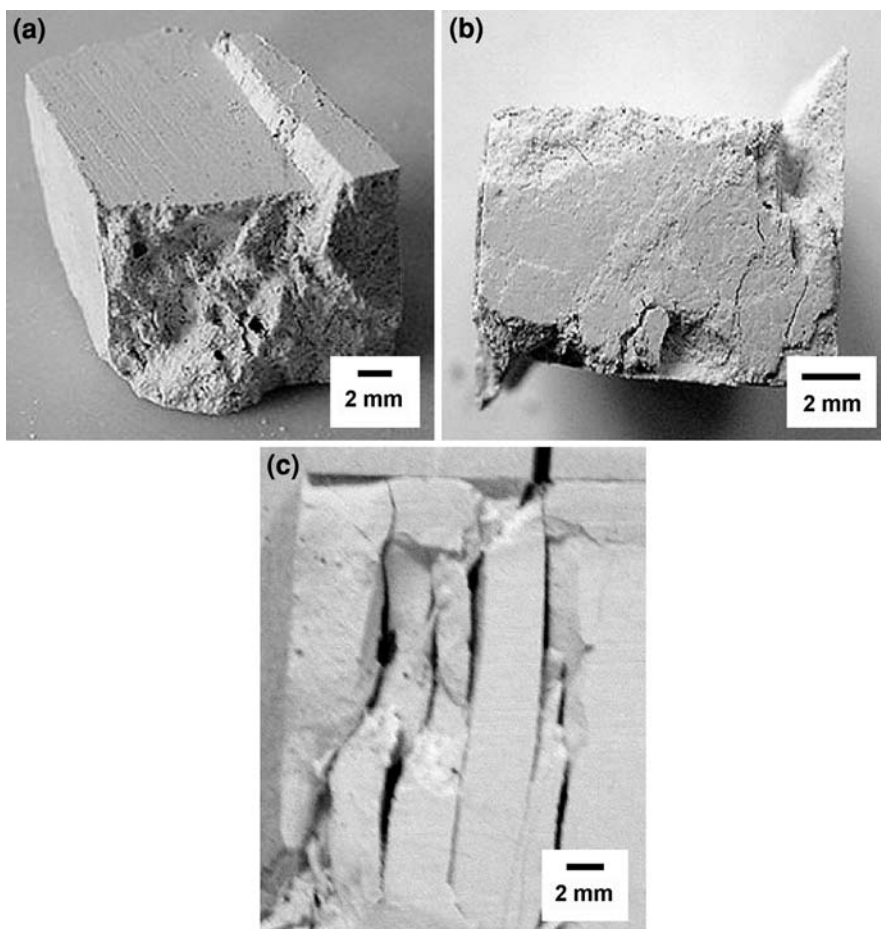
$$\rho = 68682D^{-1.08} \quad (4)$$

where  $D$  is the average size of elements.

Equation 4 implies that if a rock specimen has a smaller grain size, higher number of cracks, more damage, is required to fail the rock. In other words, grain boundaries act as crack



**Fig. 8** Different types of shear cracks observed in the present study



growth barriers and hence postpone rock failure. This is one reason behind the higher strength of fine-grained rocks.

Aspect ratio ( $L/W$ ) of the elements influences the damage level of both horizontal and vertical elements, but in different manners. Crack density in horizontal elements increases with aspect ratio according to a positive logarithmic equation,

$$\rho = 3,734Ln(L/W) + 2,236 \tag{5}$$

whereas in vertical elements crack density decreases following a negative logarithmic equation

$$\rho = -810Ln(L/W) + 1,960 \tag{6}$$

Higher damage in critically oriented elements of specimen explains for the strength anisotropy in layered rocks, i.e. strength is lower when layers are perpendicular to applied load and higher when layers are parallel to applied load.

According to Fig. 12a, a more interesting observation is that the damage level in horizontal elements themselves increases as aspect ratio increases. This implies that the long critically oriented elements take more stress than the shorter elements. More stress in longer elements means a heterogeneous stress distribution in the interlocked specimens. In fact this proves a clear association between the

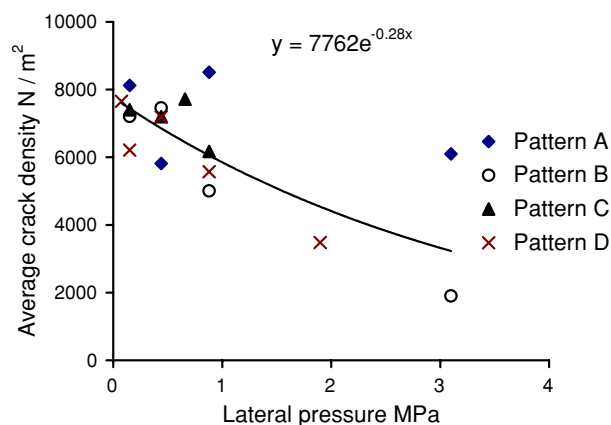


**Fig. 9** Effect of lateral pressure on the average crack density

geometrical heterogeneity of a rock and the patterns of stress distribution in that rock.

### 5.3 Failure Mechanism

Based on the observations made in the present study the brittle failure mechanism in a heterogeneous medium can be described as follows:

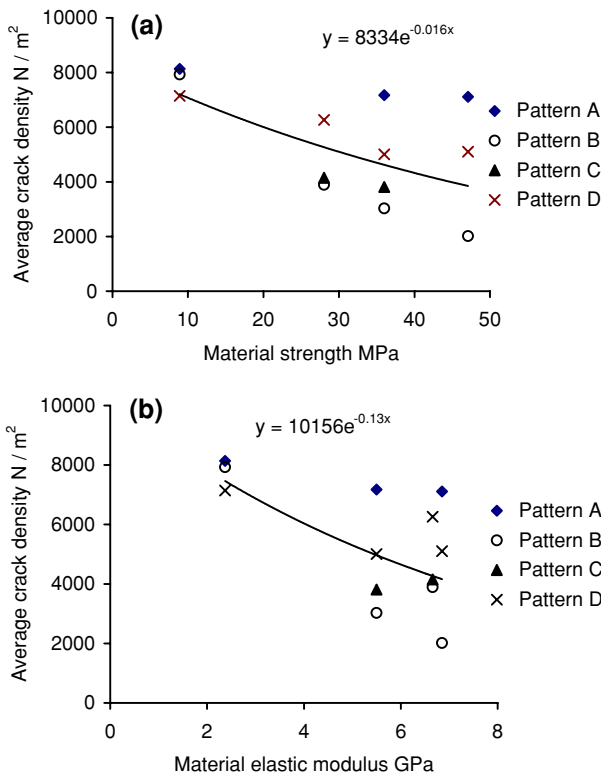


**Fig. 10** Effect of material strength and elastic modulus on the average crack density

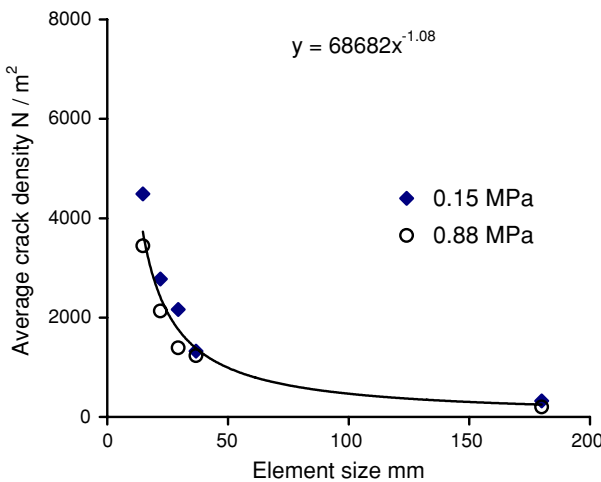


**Fig. 11** Effect of element size on the average crack density

At 10–20% of peak load, first tensile cracks are observed in horizontal lengthy elements extended perpendicular to the maximum principal stress (Fig. 13). These cracks gradually grow parallel to the major principal stress and become more visible. With increasing applied load, new cracks start at the shorter or thicker elements extended perpendicular to the major principal stress. After some growth, these cracks stop at the elements boundaries.

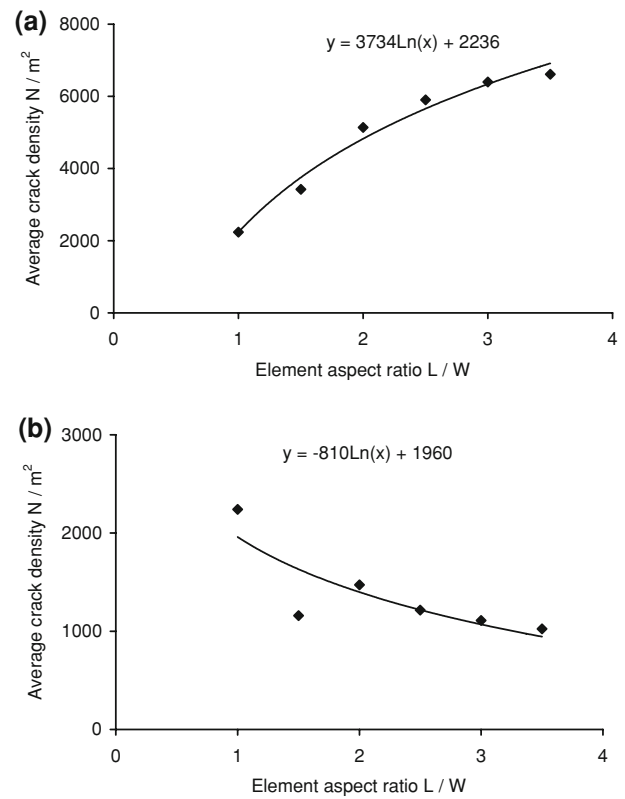


**Fig. 12** Effect of aspect ratio of **a** horizontal and **b** vertical elements on the average crack density



**Fig. 13** First tensile cracks observed in the lengthy horizontal elements

At 25–50% of peak load, second crack in the same element is observed parallel to an already existing tensile crack as shown in Fig. 14.

At 50–60% of peak load, first tensile cracks are observed in equidimensional elements having  $L/D \approx 1$ . At the same time elements boundaries start widening.

At 60–70% of peak load crack extension occurs, i.e. cracks that have already reached the elements boundaries extend further and cross the neighbouring elements as



**Fig. 14** Double cracking in the lengthy horizontal elements

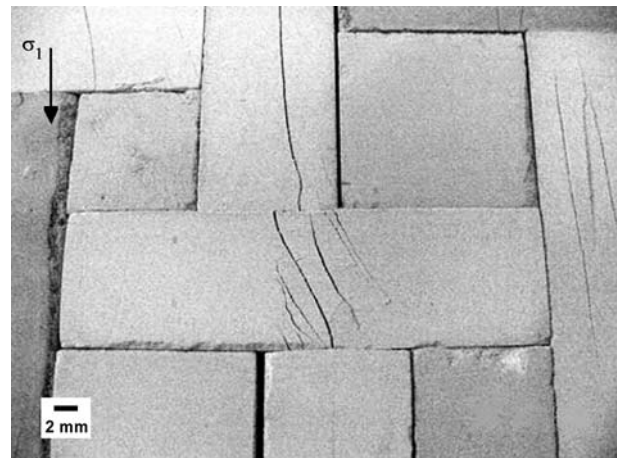


**Fig. 16** Multiple cracking in the lengthy horizontal elements

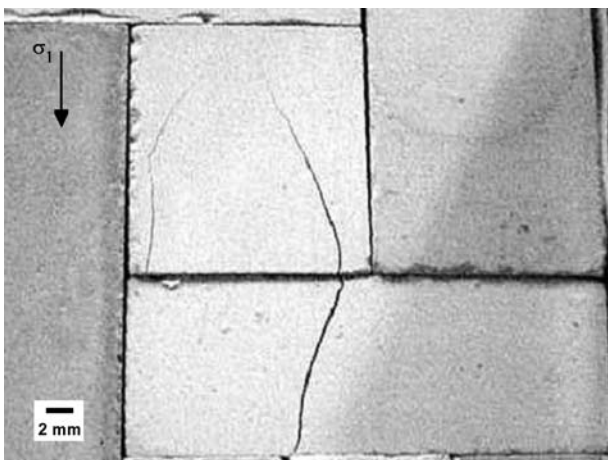


**Fig. 15** Crack extension beyond horizontal elements

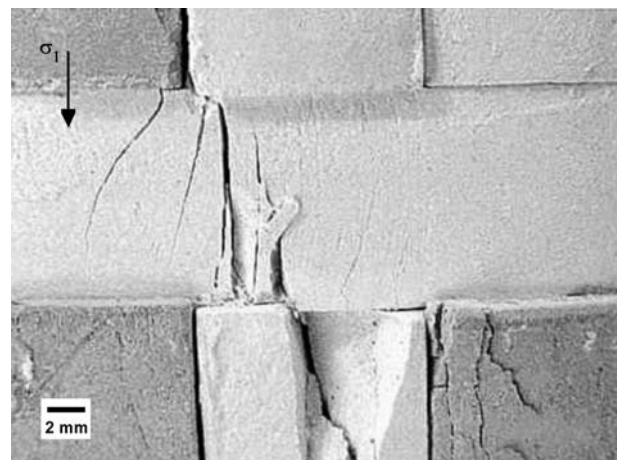


**Fig. 17** Microbuckling phenomenon observed near the peak strength

depicted in Fig. 15. Simultaneously, two other incidents occur: third tensile crack is visible in the lengthy horizontal elements and first tensile crack can be observed in the lengthy vertical elements.

At 70–85% of peak load, intense tensile cracking is visible in the lengthy horizontal elements as shown in Fig. 16. Large number of parallel cracks occurs very close to each other thereby making a number of very slender columns in the loaded specimen. At the same time, two other incidents occur: crack extension continues and extended cracks cross the third element and second crack can be observed in the lengthy vertical elements.

At 90% of peak load approximately, microbuckling of the slender columns of material, formed in the loaded specimen, occurs as shown in Fig. 17. This incident is very important in the overall failure of the specimen and is not easily observable. It happens over a very short period and immediately shifts into a shear phenomenon. Almost

simultaneously, some shear signs therefore come to the picture. Shear signs observed in this study are:

1. chipping out of the small pieces of material,
2. clear shear sound in the specimen,
3. traces of shear, and
4. bending of the element surface.

At 95% of peak load approximately, local shears take place in the specimens as shown in Fig. 18. This phenomenon reveals itself in two ways: clear shear sound and sudden but minor load drop.

At 100% of peak load, ultimate failure occurs followed by a clear shear sound and a major load drop (Fig. 19).

#### 5.4 New Critical Observations

Excluding expected observations in the process of brittle failure, there are a number of significant original observations emerged in the present study that clarify and improve the current awareness of the brittle failure process.



**Fig. 18** Shearing fracture passing through a series of tensile cracks

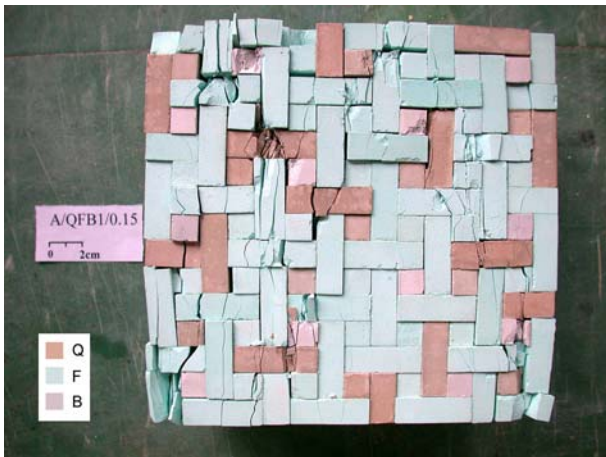


**Fig. 19** A failed specimen after applying peak load

Reviewing the literature on brittle failure gives a vision that the failure is a continuing process that starts with microcrack initiation, continues with crack growth, propagation and interaction and leads to the macroscopic failure, consequence of cracks coalescence (Blair and Cook 1998). In other words, the current understanding assumes that the microcracks grow and join at the ends to form a macroscopic failure plane. The observations of the present study reconfirm the events of crack initiation and growth but regarding the interaction and coalescence stages give a different and novel view.

As mentioned earlier, crack initiation in the tested specimens starts about maximum 20% of the peak load. After initiation, cracks grow as load increases but the growth is conversely stable as observed here and mentioned by Ashby and Hallam (1986). Most of the cracks stop at building element (grain) boundaries and few cracks that cross the boundaries usually stop after crossing two or three elements (grains).

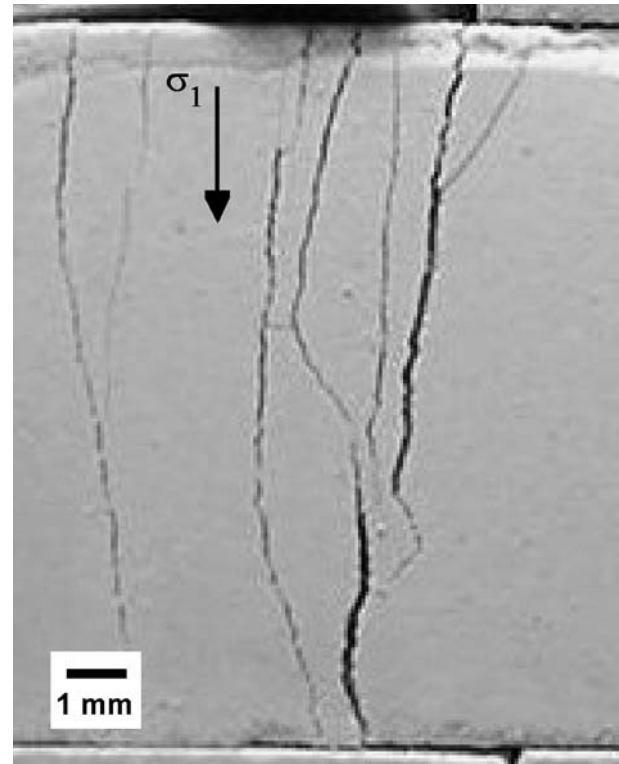


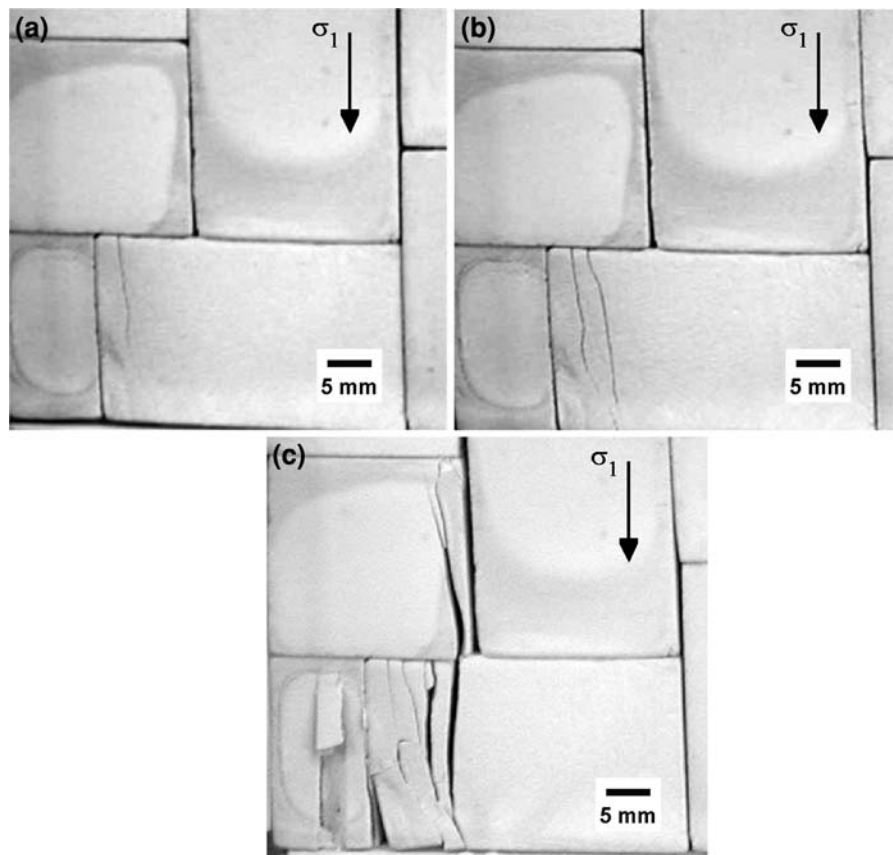
**Fig. 20** Multiple parallel cracking phenomenon observed in horizontal elements

As a new observation in the present study, there exists the phenomenon of crack population rather than the random crack growth or propagation, i.e. after limited growth of a crack, a new crack kicks off parallel and close to the first crack (Fig. 20). The small gap between parallel cracks decreases as the applied load increases.

The most significant observation is an unnoticed incident in the failure process that plays the key role of connecting the microscopic and stable tensile cracking phenomenon to the macroscopic unstable shearing phenomenon. This incident is the microbuckling of very slender columns of material formed amid of closely located tensile cracks. The sequence of events that leads to the microbuckling is shown in Fig. 21.

Just upon occurrence of microbuckling, a shear momentum builds up in the specimen that drives the neighbouring columns to cut off. By shearing each column the shear momentum, which is backed by the axial applied load, increases and the shear movement accelerates. In a very short time, the instability shows itself in the form of a macroscopic failure plane. This plane is a shear surface that passes across tensile cracks at initial stages but, after some growth, it may also pass along some favourably oriented tensile cracks and element (grain) boundaries. In this case, the clean surface of tensile cracks will turn into earthy-like surfaces as shown in Fig. 7.

**Fig. 21** **a** First tensile crack at 10–20% of peak load, **b** double cracking at 40–70% of peak load, and **c** extensive cracking and microbuckling phenomenon at >90% of peak load



In summary according to the new observations made in the present study, the stages of brittle failure can be restated in the following order:

1. microcrack initiation,
2. microcrack systematic propagation,
3. microcolumns formation,
4. microcolumns collapse, and
5. macroscopic shear.

Regarding the heterogeneity effects on the brittle failure, it is observed that the stress concentration causing damage, i.e. microcracking, occurs primarily according to the general composition of the specimen. This means that the structure/skeleton of the specimen has a decisive role on the failure process. If the structure has a considerable higher modulus (stiffness) than the inferior portion, then initially the inferior will take no load and the first cracks will appear in the structure. The weaker part will take load only after gradual collapse of the structure near to the peak point. This is especially the case when the size of the softer elements is smaller than the stiffer elements as observed in the pattern A and B specimens. B-material elements in patterns A and B usually showed presence of cracks only after a large amount of damage in the stiffer elements, i.e. Q and F, had occurred. Figure 22 depicts this phenomenon and shows two B elements (small units in the centre and

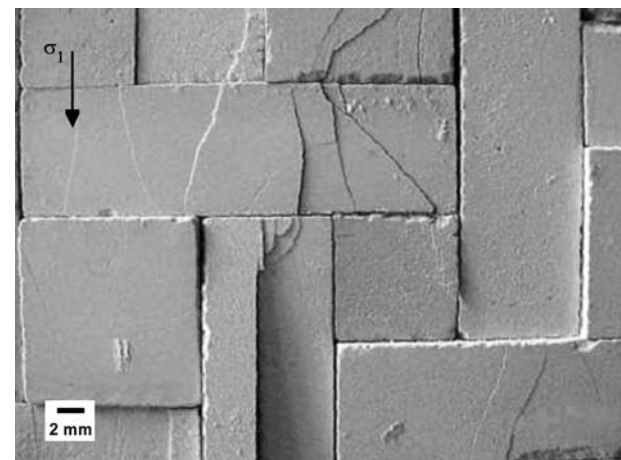


**Fig. 22** Less cracks in B-material elements (small units in the *centre* and *top-left* corner) as long as the specimen structure is not collapsed

top-left corner) that are relatively damage-free comparing to their stiffer neighbours.

On the other hand, if the structure of a specimen has a considerable lower modulus (stiffness) than the inferior, both portions will initially take load and the first cracks will appear in the weaker portion.

A second factor that greatly affects the stress distribution in a heterogeneous medium is the geometrical

characteristics of the elements. Orientation, aspect ratio and size of elements are the three factors to determine the damage level. As mentioned in the previous section, the first cracks will always appear in lengthy horizontal (perpendicular to  $\sigma_1$ ) elements. It is noteworthy to mention that the damage level, between two elements with the same orientation, does not change linearly with their lengths. The number of tensile cracks in the longer element increases exponentially relative to the shorter one. In fact, the majority of cracks in the tested specimens were observed in the horizontal lengthy elements.

### 5.5 Comparison with the Findings of Masonry Researchers

As mentioned in Sect. 4, the testing program of the present study is somewhat similar to the experimental studies on the strength properties of masonry structures. It is wise therefore to compare the current findings with the results already obtained in the masonry field.

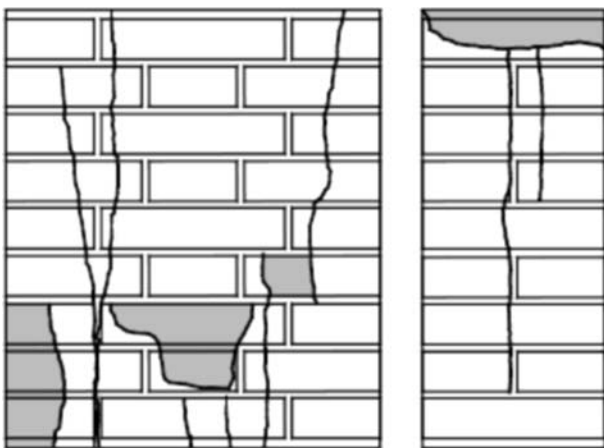
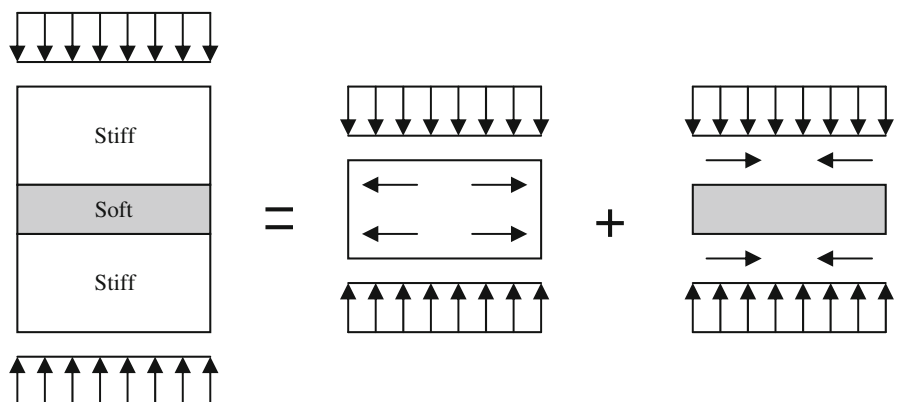


**Fig. 23** Typical failure pattern of masonry prisms under uniaxial compression loading. Face and side views are shown, the shaded areas indicate spalling of material (Frigerio and Frigerio 1985)

**Fig. 24** State of stress in masonry components under uniaxial compression of whole system



A comprehensive biaxial testing program was performed by Page (1981, 1983) on half scale solid clay bricks in both tension and compression conditions. In biaxial compression, failure typically occurred by splitting the specimen at mid-thickness, in a plane parallel to its free surface. For principal stress ratios  $\ll 1$  and  $\gg 1$ , failure occurred in a combined mechanism involving both joint failure and lateral splitting. Similar observations were made in the present study: as lateral pressure increased on the specimen, there was a transition of macroscopic failure from a plane normal to its free surface to a plane parallel to it. To avoid lateral splitting that closed visibility over the failure process, it was tried to keep the ratio  $\sigma_3/\sigma_1$  as small as possible.

Binda et al. (1988) carried out uniaxial compressive tests on masonry prisms with dimensions of  $600 \times 500 \times 250 \text{ mm}^3$ , built up with the nine courses of  $250 \times 120 \times 55 \text{ mm}^3$  soft mud bricks and 10 mm thick mortar joints. The obtained failure patterns (Fig. 23) show close similarities with the failure patterns observed in the present study (Fig. 19). However, the current study has given a much more detailed description of the failure process.

In a pioneering work, Hilsdorf (1969) demonstrated that, assuming the compatibility of strains, uniaxial compression of masonry leads to a state of triaxial compression in the mortar (weaker) and of biaxial compression/tension in the brick (stronger) as shown in Fig. 24. In view of the above conclusion, the early tensile cracking of stronger elements, i.e. Q and F in Fig. 6a, b, is the effect of biaxial compression/tension and later shear cracking of weaker elements, i.e. B in Fig. 8a, b is a result of triaxial compression in weaker elements (it should be noted that the present biaxial testing program could be fairly considered as a uniaxial testing since the magnitude of  $\sigma_3$  is quite low).

As an alternative modelling tool, a vast amount of numerical modelling efforts have been undertaken in recent years in the masonry field. Lourenço (1996) has compared different modelling strategies and grouped them into

micro-modelling strategy, where joints are modelled with zero-thickness interface elements, and a macro-modelling strategy, where an assumption of a homogeneous material is made. For the purpose of the present study, i.e. the study of failure process, a micro-modelling approach is preferred. The micro-modelling itself can be carried out using continuum-based numerical methods, i.e. finite elements, or discontinuum-based numerical methods, i.e. distinct elements. Lourenço and Pina-Henriques (2006) used continuum numerical models to reproduce the experimental compressive behaviour of masonry, but observed that the continuum finite element modelling largely overestimates the strength and peak strain of the specimens. In view of the above study, the authors of the current paper conclude that a completely discontinuum-based modelling approach will be preferred if a further numerical modelling of the present study is sought.

## 6 Conclusions

In total 66 specimens are tested at four lateral pressures, four interlocking patterns and with different configurations of element types.

Cracks observed in the present study are predominantly tensile. The distinctive characteristic of these cracks is their direction that is sub-parallel to the major principal stress. Observed tensile cracks can be roughly categorised into six groups:

1. sharp straight cracks,
2. simple curved cracks,
3. complex curved cracks,
4. sharp-branched cracks,
5. curved-branched cracks,
6. combined cracks.

In addition to the tensile cracks, essentially shear type cracks were formed in the brittle specimens and observed at the last stages of loading.

### 6.1 Parameters Affecting Crack Density

The crack sheets prepared for all specimens are examined and number of cracks within each element of each specimen are counted. Density data are arranged with respect to the material type and size of elements for all specimens. Effective parameters on crack density are found after inspecting density values against several potential factors. The following parameters are thus found to influence crack density:

1. lateral pressure,
2. material strength,

3. material elastic modulus,
4. element size,

(crack density reduces with each of the above parameters following a linear relationship)

5. element aspect ratio: crack density increases with aspect ratio following a nonlinear relationship, for elements that are perpendicular to the major principal stress. However, for elements that are parallel to the major principal stress the situation is vice versa.

### 6.2 Brittle Failure Mechanism

As Blair and Cook (1998) concluded from previous studies, the brittle failure process starts with microcrack initiation, continues with crack growth and interaction and leads to the macroscopic failure in consequence of cracks coalescence. The present study reaffirms occurrence of the crack initiation and growth but relating to the crack interaction and coalescence stages provides a different and novel view. In summary, according to the results of the present study, the stages of brittle failure can be restated in the following order:

1. microcrack initiation,
2. microcrack systematic propagation,
3. microcolumns formation,
4. microcolumns collapse, and
5. macroscopic shear.

**Acknowledgments** The content of this paper is part of the PhD program of the first author. This work was financially supported by the University of Birjand, Iran. The authors greatly acknowledge the University of Birjand for the continuous support provided all through this work.

## References

- Ashby MF, Hallam SD (1986) The failure of brittle solids containing small cracks under compressive states. *Acta Metall* 34:497–510
- Barth TFW (1952) *Theoretical petrology*. Wiley, New York, p 387
- Baud P, Klein E, Wong TF (2004) Compaction localization in porous sandstones: spatial evolution of damage and acoustic emission activity. *J Struct Geol* 26:603–624
- Belikov BP (1967) Plastic constants of rock-forming minerals and their effect on the elasticity of rocks. In: Zalesskii BV (ed) *Physical and mechanical properties of rocks*. Academy of Sciences of the USSR, Israel Program for Scientific Translations, Jerusalem, pp 124–140
- Bieniawski ZT (1967) Mechanism of brittle fracture of rock. *Int J Rock Mech Min Sci* 4:395–430
- Binda L, Fontana A, Frigerio G (1988) Mechanical behaviour of brick masonries derived from unit and mortar characteristics. In: *Proceedings of the eighth international brick/block masonry conference*, Dublin, Ireland, pp 205–216

- Blair SG, Cook NGW (1998) Analysis of compressive fracture in rock using statistical techniques: Part I. A non-linear rule-based model. *Int J Rock Mech Min Sci* 35:837–848
- Bowen NL (1915) Crystallization-differentiation in silicate liquids. *Amer J Sci* 39:175–191
- Bruland A (1998) Hard rock tunnel boring, vol 8. Ph.D. Thesis, Norwegian University of Science and Technology, Trondheim, pp 17
- Cook NGW (1965) The failure of rock. *Int J Rock Mech Min Sci* 2:389–403
- Dorner D, Stöckhert B (2004) Plastic flow strength of jadeite and diopside investigated by microindentation hardness tests. *Tectonophysics* 379:227–238
- Frigerio G, Frigerio P (1985) Influence of the components and surrounding environment in the mechanical behaviour of brick masonry [in Italian]. Graduation thesis. Politecnico di Milano, Italy
- Hallbauer DK, Wagner H, Cook NGW (1973) Some observations concerning the microscopic and mechanical behaviour of quartzite specimens in stiff, triaxial compression tests. *Int J Rock Mech Min Sci Geomech Abstr* 10:713–726
- Hilsdorf H (1969) An investigation into the failure mechanism of brick masonry loaded in uniaxial compression. In: Johnson FB (ed) *Designing, engineering and construction with masonry products*. Gulf Publishing Company, Houston, pp 34–41
- Irvine TN (1982) Terminology for layered intrusions. *J Petrol* 23:127–162
- ISRM (1978) Suggested methods for determining the strength of rock materials in triaxial compression. *Int J Rock Mech Min Sci Geomech Abstr* 15:99–103
- ISRM (1979) Suggested methods for determining the uniaxial compressive strength and deformability of rock materials. *Int J Rock Mech Min Sci Geomech Abstr* 16:135–140
- Johnson KL (1985) *Contact mechanics*. Cambridge University Press, London, p 456
- Knittle E (1995) Static compression measurements of equations of state. In: Ahrens TJ (ed) *Mineral physics and crystallography: a handbook of physical constants*. American Geophysical Union Press, Washington DC, pp 98–143
- Kranz RL (1979) Crack–crack and crack–pore interactions in stressed granite. *Int J Rock Mech Min Sci Geomech Abstr* 16:37–47
- Lockner DA, Byerlee JD (1977) Acoustic emission and fault formation in rocks. In: Hardy HR, Leighton FW (eds) *Proceedings of 1st conference on acoustic emission microseismic activity in geological structures and materials*. Trans-Tech Publications, Clausthal-Zellerfeld, pp 99–107
- Lourenço PB (1996) *Computational strategies for masonry structures*. Ph.D. thesis. Delft University of Technology, The Netherlands. Available from [www.civil.uminho.pt/masonry](http://www.civil.uminho.pt/masonry)
- Lourenço PB, Pina-Henriques J (2006) Validation of analytical and continuum numerical methods for estimating the compressive strength of masonry. *Comput Struct* 84:1977–1989
- Marder M, Fineberg J (1996) How things break. *Phys Today* 49:24–29
- Martin D, Griffiths W, Campbell IH (1987) Compositional and thermal convection in magma chambers. *Contrib Mineral Petrol* 96:465–475
- Menéndez B, Zhu W, Wong TF (1996) Micromechanics of brittle faulting and cataclastic flow in Berea sandstone. *J Struct Geol* 18:1–16
- Nemat-Nasser S, Horii H (1982) Compression-induced nonlinear crack extension with application to splitting, exfoliation, and rockburst. *J Geophys Res* 87:6805–6821
- Noferesti H (2007) *Simulation of brittle failure in crystalline rocks*. Ph.D. thesis. Indian Institute of Technology Delhi, India
- Page AW (1981) The biaxial compressive strength of brick masonry. *Proc Inst Civ Eng* 71(Part 2):893–906
- Page AW (1983) The strength of brick masonry under biaxial compression-tension. *Int J Mason Constr* 3:26–31
- Peng S, Johnson AM (1972) Crack growth and faulting in cylindrical specimens of Chelmsford granite. *Int J Rock Mech Min Sci* 9:37–86
- Philpotts AR (1990) *Principles of igneous and metamorphic petrology*. Prentice-Hall, London, p 498
- Rao KS, Tiwari RP (2004) A polyaxial testing system for prediction of engineering behaviour of jointed rock and rock mass. *ASTM Geotech Test J* (Paper ID ENGE 01672 accepted)
- Reches Z, Lockner DA (1994) The nucleation and growth of faults in brittle rocks. *J Geophys Res* 99:18159–18174
- Reyes O, Einstein HH (1991) Fracture mechanism of fractured rock, a fracture coalescence model, vol 1. In: *Proceedings of the Seventh Congress of ISRM, Aachen, Germany*, pp 333–340
- Sprunt ES, Brace WF (1974) Direct observation of microcavities in crystalline rocks. *Int J Rock Mech Min Sci Geomech Abstr* 11:139–150
- Wager LR, Brown GM, Wadsworth WJ (1960) Types of igneous cumulates. *J Petrol* 1:73–85
- Wong TF (1982) Micromechanics of faulting in Westerly granite. *Int J Rock Mech Min Sci Geomech Abstr* 19:49–64
- Wu XY, Baud P, Wong TF (2000) Micromechanics of compressive failure and spatial evolution of anisotropic damage in Darley Dale sandstone. *Int J Rock Mech Min Sci* 37:143–160